Ultramicroscopy 264 (2024) 113995

Contents lists available at ScienceDirect

Ultramicroscopy

journal homepage: www.elsevier.com/locate/ultramic

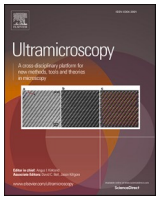

Reaction-diffusion study of electron-beam-induced contamination growth

Erich Müller [a,*], Katharina Adrion [a], Milena Hugenschmidt [a,b], Dagmar Gerthsen [a]

[a] Laboratory for Electron Microscopy, Karlsruhe Institute of Technology (KIT), Engesserstr. 7 76131 Karlsruhe, Germany
[b] 3DMM2O - Cluster of Excellence (EXC-2082/1 – 390761711), Karlsruhe Institute of Technology (KIT) 76131 Karlsruhe, Germany

ARTICLE INFO

Keywords:
Reaction-diffusion equation
Electron-beam-induced contamination
Electron microscopy

ABSTRACT

A time-dependent reaction-diffusion model was elaborated to better understand the dynamical growth of contamination on surfaces illuminated by an electron beam. The goal of this work was to fully describe the flow of hydrocarbon molecules, denoted as contaminants, and their polymerization in the irradiated area with the number of parameters reduced to a minimum necessary. It was considered that the diffusion process of contaminants is driven by the gradient of their surface density generated by the impact of a circular homogeneous electron beam. The contribution of the residual gas atmosphere in the instrument was described by the tendency to reestablish the initial equilibrium surface density of contaminants before irradiation. The four unknown parameters of the model, the electron interaction cross-section, the diffusion coefficient, the initial surface density of contaminants, and the frequency of the supply of contaminants from the residual gas atmosphere were determined by comparing the modeled contamination growth with experimental results. The experiments were designed such that the influence of the single parameters could be unequivocally separated. To follow the dynamical evolution of the system and to generate time-resolved distinct experimental data, successive contamination measurements were performed at short time intervals up to 20 min. The local height and shape of the grown contamination were quantified by evaluating high-angle annular dark-field (HAADF) scanning-transmission- electron-microcopy (STEM) image intensities and corresponding Monte-Carlo simulations. Our model also applies to nonhomogeneous initial conditions like the reduced local surface density of contaminants after previous beam-showering. The dynamic analyses of this process might provide hints regarding the relative size of the contaminant molecules and also indicate some measures for the reduction of contamination growth.

1. Introduction

In electron microscopy, carbonaceous contaminations deposited on the sample during electron beam irradiation degrade the quality of images. They aggravate structural and compositional analysis of the material and can lead to charging effects [1,2]. The formation of carbon contamination is documented for scanning electron microscopy (SEM) as well as for transmission electron microscopy (TEM) in several studies [1,3–11].

Contamination grows on irradiated surfaces and occurs for thin samples on both sides of the film if the electron beam can penetrate the material [12]. The contamination deposit is amorphous and carbonaceous but may also contain other elements, like hydrogen, oxygen, or nitrogen [7,10,13–15].

Contamination occurs if an electron beam with sufficiently high energy decomposes hydrocarbon molecules (denoted as contaminants in the following) on the sample surface and polymerizes them locally to contamination. Localized irradiation leads to a gradient in the concentration of the contaminants and drives a diffusion process. Several authors concluded that diffusion of surface contaminants is dominant [16–19]. Other models [20–22] consider an additional source of contaminants from the residual gas atmosphere in the instrument. Similarly, electron-beam-induced deposition (EBID) is modeled as surface diffusion with an additional source of precursor reactants [23–25].

Polymerization of carbon-rich organic molecules on sample surfaces illuminated by an electron beam is a complex process and depends on many parameters and different physical mechanisms. Considering sources of contaminants requires the knowledge of the initial surface density of contaminants on the sample and in the instrument chamber, the residual gas composition, pressure, and temperature in the microscope, as well as the adsorption and desorption frequency of the reactants [20,22]. The term that describes the interaction between electrons and contaminants (denoted as reaction term) implies the knowledge of the decomposition cross-section of the electron beam,

* Corresponding author..
E-mail address: erich.mueller@kit.edu (E. Müller).

https://doi.org/10.1016/j.ultramic.2024.113995
Received 4 December 2023; Received in revised form 19 April 2024; Accepted 25 May 2024
Available online 27 May 2024

which depends on the electron energy, current density, and the type of contaminants [25,26]. Regarding the energy dependence, the decomposition cross-section shows a maximum at around 100 eV [27], which implies that secondary electrons released close to the surface dominate the dissociation rather than the primary electrons with higher energies [17,25,28]. The dissociation process is also a function of the substrate temperature, determined by the heat dissipation of the beam [24–26,29,30]. Some authors additionally take into account the etching effect of the irradiating beam, which competes with the growth of contamination [24,25,30]. The mobility of the contaminants on surfaces depends on the diffusion constant, which is a function of temperature and the local heat dissipation of the electron beam [25]. This vast number of parameters, some of which are not accessible, others dispersed in a wide range of values or mutually dependent [18], complicates the validation of the models and the understanding of the contamination process.

The growth of contamination is a dynamic process, generally described by time-dependent reaction-diffusion considerations. The model developed by Müller [20] describes the change of the area density of molecules on the surface N as a function of time t by the following differential equation:

$$\frac{\partial N}{\partial t} = \underbrace{\frac{P}{\sqrt{2\pi m k_B T}}}_{adsorption} - \underbrace{\frac{N}{\tau_0}}_{desorption} - \underbrace{\frac{\xi(E_0)\cdot J}{e}\cdot N}_{reaction\ \ term} + \underbrace{D\cdot\Delta N}_{diffusion}, \tag{1}$$

with partial pressure P of contaminants, molecular mass m of the contaminants, Boltzmann constant k_B, temperature T, residence time τ_0 of molecules on the surface, primary electron energy E_0, electron beam interaction cross-section $\xi(E_0)$ including decomposition and cross-linking of the contaminants and electron beam-driven desorption, electron beam current density J, electron charge e, diffusion constant D, and the Laplace operator Δ.

Several theoretical models describe the process of beam-induced deposition, the challenge being to solve the time-dependent reaction-diffusion equation with consideration of an additional source of reactants. Müller [20] and Agmon [31] provided an analytical solution by assuming a steady-state equation $\frac{\partial N}{\partial t} = 0$. Kanaya et al. [29] and Amman et al. [16] solved the time-dependent surface diffusion equation by considering a uniform reaction term within the illuminated area. Excluding an additional source of reactants, Rykaczewski et al. [17] solved the diffusion equation with a time-dependent reaction term by the finite difference method. In addition, Monte-Carlo (MC) methods are used to simulate electron-beam-induced deposition (EBID) processes [23,30,32,33].

There are also special techniques like beam-showering for suppressing contamination, which cannot be treated in terms of stationarity. Beam-showering is a method to reduce the initial density of contaminants in a large area surrounding the region of interest [13,16,18,34]. The subsequent flow of contaminants through the depleted area depends on time and is governed by parameters like their surface diffusion coefficient.

In this work, we describe the contamination process in a time-dependent surface diffusion model by unambiguous parameters, which are known or are determined by adjusting the simulation to experimental results. To reduce the number of parameters, some of the individual terms from Eq. (1) are merged into a single one. Several parameters, like beam energy and current, illuminated area, and electron beam exposure time are measured in our experimental setup. The unknown parameters are determined by comparing the predictions of the model with the results of experiments. Starting from typical values found in the literature, they are adjusted to fit the predicted contamination thickness profiles to the measured ones. It is found that the diffusion coefficient, the beam reaction cross-section, the initial density of surface contaminants, and their adsorption frequency from the residual gas are independent parameters and can be determined in this way. We consider these parameters in our time-dependent surface diffusion model to describe the dynamics of contamination formation and to determine the flow of contaminants with different initial and boundary conditions. The resulting inhomogeneous reaction-diffusion equation is solved similarly to the calculations for the bio-heat equation of Giordano et al. [35] by the method of fundamental solutions in cylindrical coordinates. Results are calculated numerically for distinct time intervals.

We have validated our model by experiments conducted in a scanning electron microscope, where contamination was grown by illuminating circular areas on thin carbon films with a homogeneous electron beam. The local thickness and morphology of contamination patterns were quantified similarly to the method described by Hugenschmidt et al. [18] by evaluating HAADF-STEM images and corresponding MC simulations. The parameters of our model were adjusted accordingly to obtain contamination thickness profiles in agreement with the experiments.

2. Reaction-diffusion model for contamination growth

2.1. Theoretical considerations

Following the approach of Müller [20] and starting from Eq. (1), the evolution in time t of the surface density of contaminants $N(r,t)$ on a locally illuminated surface is considered to be governed by the 2-dimensional diffusion equation. Furthermore, the relative density of contaminants $n = N/N_0$, normalized to the initial density $N_0 = N(t = 0)$ is introduced. The individual reactions of the irradiating electrons with the contaminants, like dissociation and desorption, are combined into a reaction-frequency parameter σ, similar to the reaction term in Eq. (1). Contributions of contaminants from the gaseous environment are considered by a source term η, which describes the adsorption frequency of contaminants from the residual gas. This jointly includes the contribution of adsorption of contaminants from the partial gas pressure and residence time of the contaminants, explicitly contained in Eq. (1). Unlike the meaning of the two first terms in Eq. (1) and following Utke et al. [24] and Smith [23], it is assumed that the supply from the residual gas tends to replace the local deficit of contaminants on the sample surface and to restore the initial equilibrium density $N/N_0 = 1$ before illumination, as expressed by $\eta\cdot(1 - n)$.

With these terms, the reaction-diffusion equation writes:

$$\frac{\partial n}{\partial t} = D\cdot\Delta n - \sigma\cdot n + \eta\cdot(1 - n) \tag{2}$$

D is the diffusion coefficient and Δ the Laplace operator in cylindrical coordinates for radial symmetry:

$$\Delta = \frac{\partial}{\partial r^2} + \frac{1}{r}\cdot\frac{\partial}{\partial r} \tag{3}$$

The reaction frequency σ of the electron beam relates to the number of secondary electrons generated in the illuminated area $S = \pi\cdot R^2$ of radius R and the cross-section σ_c, for the reaction of the electrons with contaminants [17] and is given by:

$$\sigma = \sigma_c\cdot\frac{j}{eS}\cdot 2\delta_E \tag{4}$$

j is the primary beam current, δ_E the secondary electron yield, and $e = 1.6\cdot10^{-19}$ C the elementary charge. A factor of 2 is inserted here to account for secondary electron generation on both sides of the illuminated film. Unlike the reaction term in Eq. (1), here the dissociation of contaminants is related by σ explicitly to the generation of secondary electrons, which also includes the dependency on the primary electron beam energy. σ_c comprises in our model dissociation (leading to deposition) and desorption of the contaminants and depends on the type of the contaminants [25,26].

With the notation $\gamma = (\sigma + \eta)$ Eq. (2) rewrites in a more convenient form:

$$\left(\frac{\partial}{\partial t} - D\cdot\Delta + \gamma\right) n(r,t) = \eta \tag{5}$$

Similar to Giordano et al. [35], we construct a solution of this equation by using Green's formalism.

The 2-dimensional fundamental solution $U(\boldsymbol{r}, \boldsymbol{r'}, t, t')$ of the equation

$$\left(\frac{\partial}{\partial t} - D\cdot\Delta + \gamma\right) U(\boldsymbol{r}, \boldsymbol{r}', t, t') = \delta(\boldsymbol{r} - \boldsymbol{r}')\delta(t - t') \tag{6}$$

with a point source at $\boldsymbol{r}'$ and t' is

$$U(\boldsymbol{r}, \boldsymbol{r}', t, t') = \frac{\delta(t-t')}{4\pi D\cdot(t-t')} e^{-\left\{\frac{(\boldsymbol{r}-\boldsymbol{r}')^2}{4D(t-t')} + \gamma(t-t')\right\}} = G(\boldsymbol{r}, \boldsymbol{r}', t, t')\cdot e^{-\gamma(t-t')} \tag{7}$$

where the Green's function

$$G(\boldsymbol{r}, \boldsymbol{r}', t, t') = \frac{\delta(t-t')}{4\pi D\cdot(t-t')} e^{\frac{-(\boldsymbol{r}-\boldsymbol{r}')^2}{4D(t-t')}} \tag{8}$$

is a solution of the diffusion equation without reaction and sources/sinks

$$\left(\frac{\partial}{\partial t} - D\cdot\Delta\right) G(\boldsymbol{r}, \boldsymbol{r}', t, t') = \delta(\boldsymbol{r} - \boldsymbol{r}')\delta(t - t'). \tag{9}$$

For cylindrical coordinates, the Green's function is given by

$$G(r, r', t, t') = \frac{\delta(t-t')}{2D\cdot(t-t')} e^{-\frac{r^2+r'^2}{4D(t-t')}} \cdot I_0\left(\frac{rr'}{2D(t-t')}\right) \tag{10}$$

where I_0 represents the modified Bessel function.

The fundamental solution for the reaction-diffusion equation then writes:

$$U(r, r', t, t') = \frac{\delta(t-t')}{2D\cdot(t-t')} e^{-\left\{\frac{r^2+r'^2}{4D(t-t')} + \gamma(t-t')\right\}} \cdot I_0\left(\frac{rr'}{2D(t-t')}\right) \tag{11}$$

With this fundamental solution, the initial conditions $n'(r') = n(r', t' = 0)$ and a source η, a solution of the reaction-diffusion equation (Eq. (2)) is constructed:

$$n(r,t) = \int_0^\infty U(r, r', t, t' = 0)\cdot n'(r')\cdot r' dr' + \int_0^t \int_0^\infty U(r, r', t, t')\cdot \eta \cdot r' dr' dt' \tag{12}$$

The second integral represents the time integration of the source η:

$$\int_0^t \int_0^\infty U(r, r', t, t')\cdot \eta \cdot r' dr' dt' = \eta \int_0^t \int_0^\infty G(r, r', t, t')\cdot e^{-\gamma(t-t')} \cdot r' dr' dt' \tag{13}$$

The integral over time t' of the product of a time-dependent Green's function and the term $e^{-\gamma(t-t')}$ represent the solution of the equation

$$\frac{\partial y}{\partial (t-t')} = e^{-\gamma(t-t')} \tag{14}$$

yielding $y = \frac{1}{\gamma}(1 - e^{-\gamma t})$ for t'=0.

Thus, the solution of the time-dependent inhomogeneous reaction-diffusion equation (Eq. (2)) becomes:

$$\begin{aligned} n(r,t) &= \int_0^\infty G(r, r', t) e^{-\gamma t} \cdot n'(r') \cdot r' dr' + \frac{\eta}{\gamma} \int_0^\infty G(r, r', t) \cdot (1 - e^{-\gamma t}) \cdot r' dr' \\ &= \int_0^\infty G(r, r', t) \cdot \left(\frac{\eta}{\gamma} + \left(n'(r') - \frac{\eta}{\gamma}\right) e^{-\gamma t}\right) \cdot r' dr' \end{aligned} \tag{15}$$

2.2. Numerical calculation of the reaction-diffusion equation

We calculated the solution (Eq. (15)) of the reaction-diffusion equation (Eq. (2)) numerically by code written in Python [36]. The relative density of contaminants $n(r,t)$ was determined for time intervals τ by applying beam reaction, residual gas supply, and the diffusion term on the local initial conditions $n'(r')$. For the very first step, the initial conditions $n'(r', t' = 0) = 1$ relate to N_0 and represent the equilibrium surface density for a homogeneous initial distribution of the contaminants. The density of contaminants $n(r,t)$ calculated after each time step then served as initial conditions for the subsequent step. The time evolution of contaminants was tracked in this way for distinct time steps up to the total observation time corresponding to the experimental measurements.

The examination of the experimental results shows that the beam reaction frequency σ is substantially larger than the adsorption frequency η from the residual gas. Also, for time intervals of τ =1 s the diffusion length is much smaller than the diameter of the illuminated area as shown in Section 4.2. Thus, for time intervals τ, which are sufficiently small to consider only the beam reaction term in Eq. (2), the density of remaining contaminants after reacting with the beam after a time interval τ is given by $n_\tau \cdot e^{-\sigma\tau}$ as the solution of the equation $\frac{\partial n}{\partial \tau} = -\sigma \cdot n$. Then the density X of the contaminants which have been dissociated after the time τ due to the beam reaction is the difference between the initial and the remaining density

$$X = n_\tau \cdot (1 - e^{-\sigma\tau}), \tag{16}$$

where the surface density n_τ of the contaminants was calculated by Eq. (15) for the considered time step τ . This relative density X relates via n_τ to the initial surface density of contaminants N_0. Assuming that all removed contaminants are polymerized, the contamination thickness t_c was calculated by

$$t_c = \frac{A}{N_A \cdot \rho} \cdot X N_0, \tag{17}$$

where we adopted the atomic mass $A = 12$ and the density ρ =1.6 g/cm^3 for pure carbon, in analogy to the results found by Hugenschmidt et al. [18]. N_A is the Avogadro constant.

Etching of contamination can be considered by reducing X in Eq. (17) accordingly by a factor $(1 - b_e) < 1$, where b_e is the fraction of contamination removed by the beam. However, b_e and N_0 are interdependent parameters and cannot be determined separately. For that reason, we used in this work only N_0 as a parameter to adjust the simulated contamination profile to the experimental curve and neglected b_e.

For the parameters of the model, a wide range of values can be found in the literature. For D, values between 10^{-15} and 10^{-6} m^2/s are published [17,18,28,32], and values between $0.5\cdot10^{-20}$ m^2 and $2\cdot10^{-20}$ m^2 are suggested for the beam reaction cross-section σ_c [18,26,37]. In our work, we determined these parameters by adjusting them to fit the measurements, starting with average values from the literature. It was shown that the diffusion coefficient and the beam reaction cross-section are independent parameters of our model. The residual gas acts as a source of contaminants, tending with the frequency η to restore the initial equilibrium density N_0. We treated both η and N_0 as independent fit parameters.

To simulate experiments with preceding beam-showering, the reduced density of contaminants in a large surrounding was calculated with the corresponding parameters of the electron beam and the radius of the extended irradiated area. The remaining relative density of contaminants after beam-showering is then $0 < N/N_0 < 1$ and serves as the local initial condition for the subsequent contamination growth process.

The time steps of the calculation were connected to the inverse of the largest frequency parameter of Eq. (2), which in the case of our experiments with an illuminating beam of radius $R \approx 600$ nm was the beam

reaction frequency $\sigma = 1\ s^{-1}$ for typical values of $\sigma_c = 10^{-20}\ m^2$ [18,26,37], $j = 112$ pA and $\delta_E = 0.08$ [38] from Eq. (4). The values for the adsorption frequency $\eta \approx 0.002\ s^{-1}$ found in our work were considerably lower.

3. Experimental setup and evaluation of the measurements

SEM contamination experiments were performed in a FEI DualBeam Strata 400S, equipped with an annular STEM detector. Smooth amorphous carbon films with a thickness of 10 nm were prepared as described by Hugenschmidt et al. [18], placed on a copper grid and used as substrates for contamination growth. After inserting the grids, the measurements were started as soon as the microscope chamber pressure reached $\sim 5{\cdot}10^{-6}$ mbar. The electron beam fixed in the spot mode was defocused to illuminate the film homogeneously on a circular area mimicking TEM-illumination condition. Choosing an appropriate defocus value at the working distance of 6.2 mm, irradiation patterns with radii of 0.6 and 7 μm were obtained. Due to instrumental uncertainties in the determination of the defocus, the radius of the illuminated regions can vary slightly from the intended value from one experiment to the other. The experimentally determined radii are used in the corresponding simulations. As a consequence of the chosen illumination, ring-like contamination was obtained in concordance with previous work [20,39]. The circular contamination was grown by illuminating the carbon film for up to 20 min at the same spot in time sequences of 1 min, each followed by an interruption of 28 s for imaging the contamination in STEM mode. The extended illuminated area was chosen to distinguish the effect of the overall residual gas supply of contaminants from that of the localized contribution by diffusion. The long-term recording of contamination growth in relatively small time steps allows to separate the impact of the distinct parametric frequencies of the model.

For fast switching between defocused irradiation in spot mode and imaging in scanning mode, the corresponding instrumental settings like focus and dwell time were loaded from previously stored files. Both irradiation and imaging were performed at the electron energy of 20 keV and a current $j = 112$ pA, which was measured with a Faraday cup. Fig. 1 shows HAADF-STEM images of ring-like contamination, grown after 1 min and 10 min total irradiation time.

In analogy to the work of Hugenschmidt et al. [18], the contamination thickness was determined from HAADF-STEM images, acquired with the implemented STEM detector, which covers the scattering-range between 168 mrad and 617 mrad at a working distance of 6.2 mm. From the intensity I in each image pixel, relative measured intensities $I_{rel} = \frac{I - I_b}{I_0 - I_b}$ were calculated by subtracting the black-level intensity I_b, which is the intensity of the HAADF-STEM detector without exposure to electrons, and normalization with the intensity I_0 of the incident electron beam. I_0 was determined by directly scanning the HAADF segment of the STEM detector.

The local contamination thicknesses were determined by comparing the relative experimental intensities I_{rel} with equivalent simulated HAADF-STEM intensities $I_{rel,\ sim}$ and subsequent subtraction of the substrate thickness. Values of $I_{rel,\ sim}$ were obtained by MC modeling of the electron transmission with a modified version of NISTMonte1.2 [40], considering the support film and the contamination to consist of pure carbon with a density of 1.63 g/cm^3, as determined by Hugenschmidt et al. [18]. Thus, the HAADF-STEM images taken at distinct time intervals were transformed into thickness maps and provided radial profiles of the contamination thickness as shown in Fig. 2. It was considered that mainly the primary beam generates secondary electrons, responsible for the dissociation of contaminants, while the contribution of backscattered electrons from the very thin substrates can be neglected at the electron energy of 20 keV. Beam-broadening, possible backscattered electrons occurring from a thicker contamination ring, and occasional sample drift can lead to a broadening of the contamination ring at the border of the illuminated area. These effects were averaged by considering the radial line scans only in the area bounded by the maximum of the contamination rings, as shown in Fig. 2.

Polymerization of contaminants during the effective imaging scans of 3 s between the irradiating cycles contributes only with a small constant greyscale offset to the images. Its influence is eliminated by subtracting the image background determined in the region outside of the contaminated area.

Additionally, experiments of beam-showering were performed by irradiating a larger area with the electron beam and subsequently

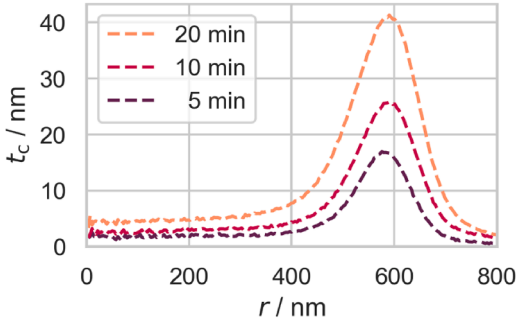

Fig. 2. Temporal evolution of contamination growth. Experimentally measured contamination thickness t_c as a function of the distance r from the center, after irradiating an area with radius $R = 580$ nm for 5, 10, and 20 min, in steps of 60 s with interruptions of 28 s for image acquisition.

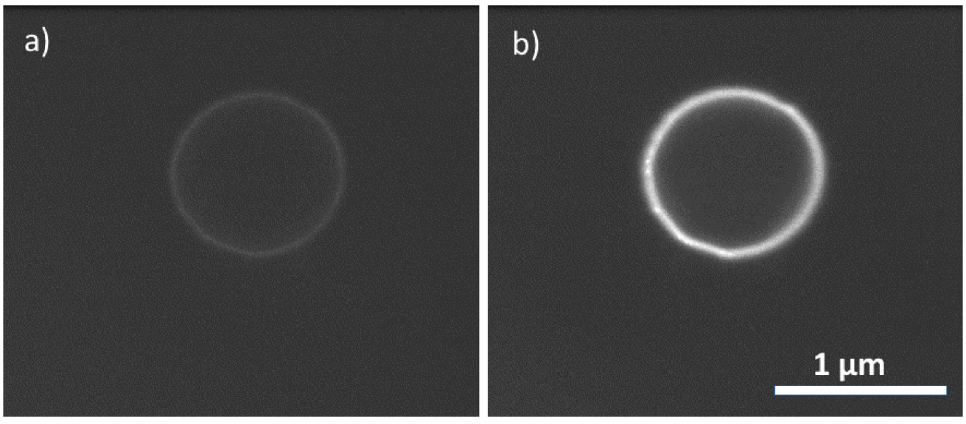

Fig. 1. HAADF-STEM images of ring-like contamination grown after (a) 1 min and (b) 10 min irradiation time respectively, with an electron beam current of 112 pA at 20 keV.

growing contamination in the center of this region. With a more pronounced defocusing of the electron beam in the spot size mode, a circular area with a radius of 7 µm was illuminated for 1 min at 20 keV with a current of 3.4 nA before the contamination growth cycles. This procedure aims to reduce the density of mobile contaminants available for surface diffusion by polymerization. Immediately after the beam-showering, a contamination growth cycle was started in the center of the depleted area with a total illumination time of 20 min in steps of 1 min interrupted for 28 s for imaging the sample in HAADF-STEM mode.

The experiments resulted in contamination patterns of different shapes and local thicknesses and were used for the determination of the growth parameters by comparison with the prediction of our model.

4. Results and discussion

4.1. Parametric study based on the model

Our model for reaction-diffusion-driven growth of contamination comprises several parameters. The energy and current of the electron beam, the size of the illuminated area, and the illumination time are known from the experimental setup. Other parameters like the diffusion coefficient D, the cross-section σ_c of the reaction with the electron beam, the supply frequency of contaminants from the vacuum η, and the initial density of surface contaminants N_0 are to be determined. Additionally, a parameter b_e can be considered to account for the etching of contamination and desorption of contamination by the illuminating beam. To distinguish the impact of these parameters on the shape and height of the calculated contamination thicknesses t_c, each of them is varied around a typical value taken from the literature mentioned in the previous section. Similar to the experimental setup, it is considered in the simulations that a circular area with radius $R = 620$ nm is illuminated homogeneously for 20 cycles with 60 s per cycle and an electron beam of $j = 112$ pA at 20 keV, which corresponds to a current density of 93 Am^{-2}. Between these steps, the simulations considered a period of 28 s of no irradiation, however, considering diffusion and adsorption of contaminants to mimic the time employed to image the experimental contaminated region. The short period of 3 s for imaging the contamination pattern is neglected in the simulation of the contamination growth. This is justified by considering Fig. 1(a,b) which show a similar greylevel in the region outside of the irradiated region for the images

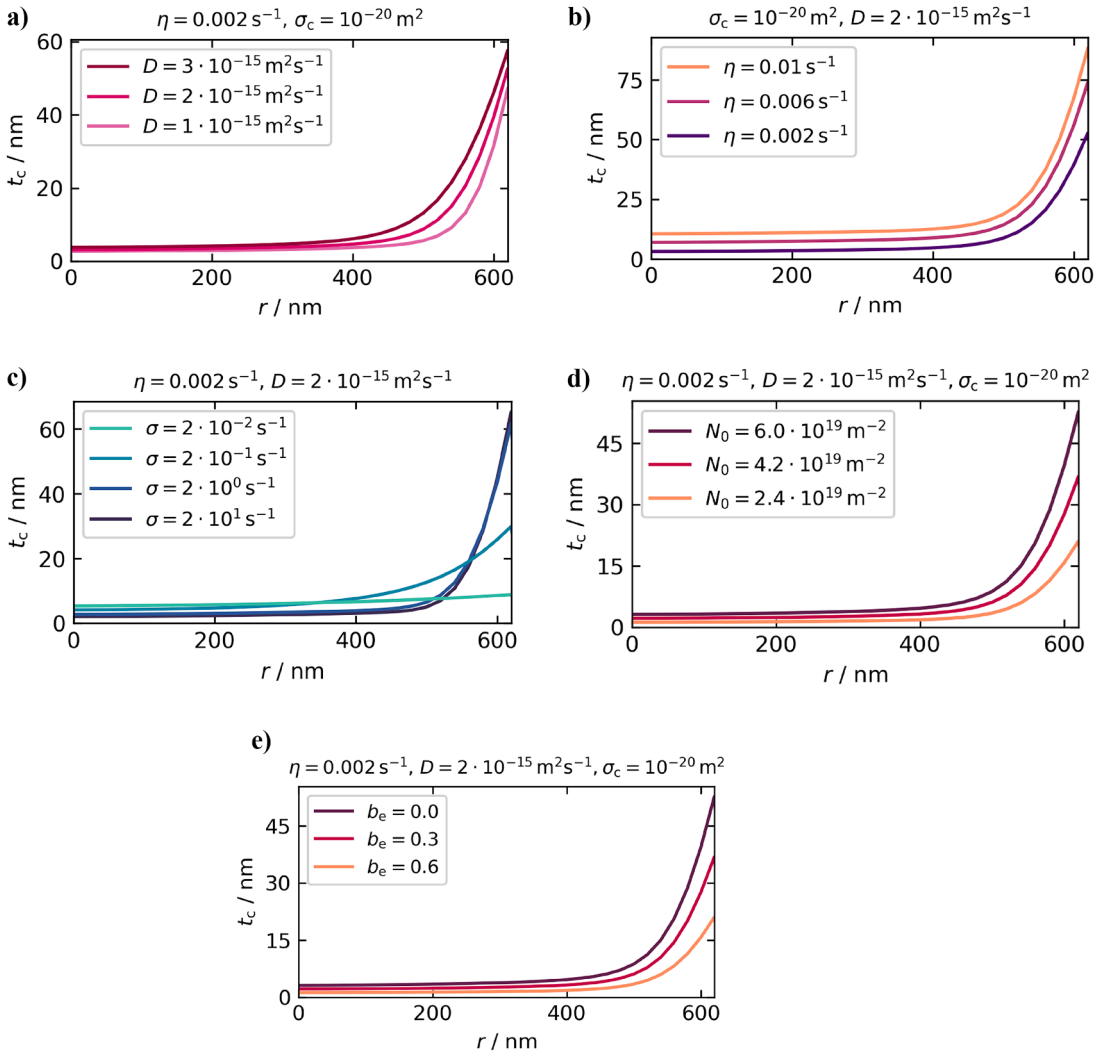

Fig. 3. Impact of the model's free parameters for a simulated total irradiation time of 20 min, in steps of 60 s with interruptions of 28 s for image acquisition. Contamination thickness t_c as a function of the distance r from the center of the irradiated area shown for variations of (a) the diffusion coefficient D, (b) the adsorption frequency η of contaminants from the residual gas, and (c) the reaction frequency σ of the electron beam with the contaminants. The subfigures (a) – (c) show the simulated results for an etching ratio of $b_e = 0$ and an initial surface density of contaminants of $N_0 = 6{\cdot}10^{19}\,m^{-2}$ corresponding to a coverage with 0.75 nm thick pure carbon film (Eq. (17)). The influence of a variation in N_0 is shown for $b_e = 0$ in (d), while the impact of the etching rate b_e on $N_0 = 6{\cdot}10^{19}\,m^{-2}$ is shown in (e). The contaminated area with a radius of 620 nm was considered to be illuminated homogeneously with a 20 keV electron beam with the current of $j = 112$ pA (except for (c), where the variation of σ implies the variation of j and σ_c).

taken after 1 and 10 min of illumination cycles.

In the following, we discuss the influence of the free parameters of the model on the simulated contamination growth. Each parameter is varied accordingly, keeping all other parameter values constant at typical values from the literature (cf. Section 2.2). A value for η is not available and was determined by comparison of simulated and experimented data ($\eta = 0.002\ s^{-1}$) as shown in Section 4.2. We assume an initial surface density of contaminants of $N_0 = 6{\cdot}10^{19}\ m^{-2}$ corresponding to a coverage with a 0.75 nm thick pure carbon film (Eq. (17)). Fig. 3 shows the thickness of the grown contamination bounded by the radius of the irradiating beam for different values of each parameter.

Already small variations of the diffusion coefficient around the value of $D = 2{\cdot}10^{-15}\ m^2s^{-1}$ have an impact on the contamination thickness, as shown in Fig. 3(a). Higher D values lead to a more pronounced contamination growth and the shape of the radial distribution of the contamination changes. The most significant change in t_c is visible close to the border of the irradiated area, whereas the influence of D is small in its center. This effect is attributed to the value of the diffusion length $L_D = \sqrt{2kDt}$, where $k = 2$ is the dimensionality of the system and t is the diffusion time [41]. Larger D results in larger L_D and more contaminants diffuse deeper into the irradiated area. For $t = 1$ s and $D = 2{\cdot}10^{-15}\ m^2s^{-1}$, the diffusion length L_D is 89 nm. This is considerably smaller than the diameter of the irradiated area. Hence, the supply of contaminants by surface diffusion is notable only at the border of the illuminated disc.

Increasing the supply of contaminants from the vacuum also increases the contamination thickness as shown in Fig. 3(b). Unlike the influence of D, the variation of the adsorption frequency η adds a constant offset to t_c all over the illuminated area, without changing the slope of the radial contamination profile. For the values of η shown here, the residual gas will mostly reestablish the equilibrium surface density of contaminants in a time between 100 and 500 s.

The influence of the cross-section σ_c for the reaction of the contaminants with the electron beam is analyzed by the arbitrary variation of the reaction frequency σ (Fig. 3(c)). Here, a distinctive change in the radial profile shape is found. Larger values of σ lead to steeper slopes at the edge of the irradiated area, while the thickness t_c is lower in the inner region, resulting in a crossing of the curves. This behavior can be understood as follows: If σ is low, a smaller number of contaminants react in a given time. The remaining contaminants can diffuse to the center of the irradiated area and lead to higher t_c. With larger σ, the irradiated area is depleted of contaminants, and diffusion can supply only the border region with new contaminants.

The number of contaminants reacting with the beam after the time t is proportional to $1 - e^{-\sigma t}$. For large σ (large σ_c or large beam currents j), all contaminants reaching the irradiated area are polymerized even for short illumination times. Thus, it is expected that saturation will occur for a sufficiently large σ. Indeed, the contamination thickness shown in Fig. 3(c) converges for the curves with $\sigma = 2\ s^{-1}$ and $20\ s^{-1}$. A similar contamination growth experiment conducted by Hugenschmidt et al. [18] has shown that a current density $j/A \sim 900\ pA/\mu m^2$ leads to saturation of the contamination growth. Inserting this saturation beam current, the secondary electron yield $\delta_E = 0.08$ [38] and $\sigma = 2\ s^{-1}$ in Eq. (4) gives the expected minimum value of the reaction cross-section $\sigma_c = 2.2{\cdot}10^{-21}\ m^2$.

The value of the initial surface concentration of contaminants N_0 does not change the shape of the thickness profile and acts as a multiplicative term for t_c as shown in Fig. 3(d). It is therefore distinguishable from the influence of the previously considered parameters. Contamination etching by the illuminating beam with the ratio b_e would act similarly as a multiplicative term as shown in Fig. 3(e) for $N_0 = 6{\cdot}10^{19}\ m^{-2}$. This contribution is expressed by a reduction of N_0 by $(1 - b_e){\cdot}N_0$ and gives identical curves for corresponding values of b_e and N_0 as shown by Fig. 3(d,e). In conclusion, N_0 and the etching rate b_e are interdependent, and cannot be fitted separately.

The results in Fig. 3(a-d) suggest that it is possible to separate the influence of D, η, σ_c, and N_0 by distinguishing the typical shape and the local height of the contamination profile. Contamination profiles recorded for each time step in the experiment serve as distinct single measurements for comparison with the model predictions. Thus, all four values are determined unequivocally by comparing simulated with experimental results of contamination growth. Due to the interdependency of N_0 and b_e, the latter is neglected and only the initial density of surface contaminants is considered in the following.

4.2. Parameter determination by comparing simulations with experimental results

The unknown parameters of the experimental setup described in Section 3 are determined by comparing simulated contamination growth with measured values of the test series.

Fig. 4(a) shows the measured radial profiles of the contamination thickness for irradiation times of 5, 10, and 20 min (dashed lines) and the corresponding simulated values (continuous lines) A logarithmic plot is chosen to highlight the pronounced differences in the thickness profile. As discussed previously, the reaction cross-section σ_c determines the steepness and relative height of the contamination curves close to the border of the irradiated area and was adjusted in the first step to fit the characteristics of the measured profiles in this area. The diffusion coefficient D, which influences the inflow of contaminants from the border and the shape of the curves towards the inner region of the illuminated circle was fitted in a second step. Already small changes of D modify the width of the contamination profiles but keep their height at the circumference of the irradiation circle almost constant. The residual gas supply frequency η uniquely adds a constant value to the height of contamination all over the irradiation zone to all profile curves. Finally, the initial density of contaminants N_0 is responsible for a multiplicative term, which affects the slope of all contamination profiles similarly and

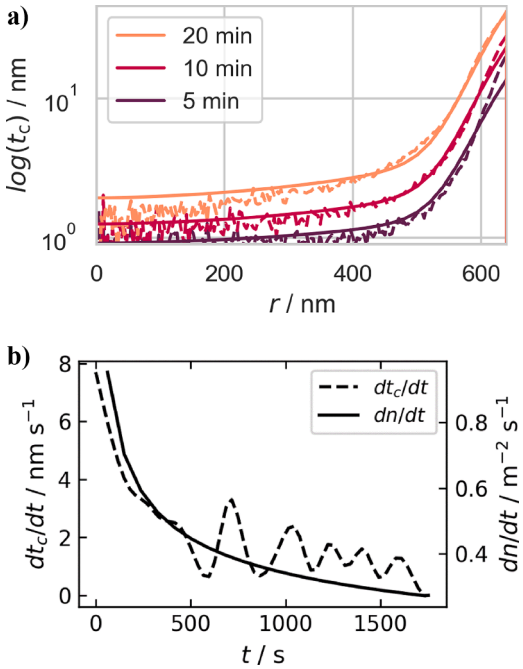

Fig. 4. (a) Experimentally measured (dashed line) and simulated (solid line) contamination thickness t_c as a function of the distance r from the center, after irradiating an area with radius $R = 640$ nm for 5, 10, and 20 min with an electron beam of $j = 112$ pA at 20 keV. Fitting the simulations to the measurements provided the parameters $D = 2{\cdot}10^{-15}\ m^2s^{-1}$, $\sigma_c = 2{\cdot}10^{-20}\ m^2$, $\eta = 0.002\ s^{-1}$ and $N_0 = 4.5{\cdot}10^{19}\ m^{-2}$. (b) Experimentally determined growth rate of contamination dt_c/dt (dashed line) and simulated rate of the density of contaminants dn/dt (solid line) at the border of the irradiated circle with the radius $R = 640$ nm after each illumination cycle.

is adjusted last. Considering these characteristics one by one, the four parameters can be determined independently for each experiment. Due to the consecutive adjustment of the simulation parameters and the high number of measured curves only qualitative fits and comparisons are implemented. As mentioned before, most important for these qualitative fits is the region of the curves closer to the border of the illuminated area and the logarithmic plot should not lead to an overestimation of the inner region. Good agreement of simulation and experiment is found for the experimental results depicted in Fig. 4(a) by setting $D = 2\cdot 10^{-15}$ m^2s^{-1}, $\sigma_c = 2\cdot 10^{-20}$ m^2, $\eta = 0.002$ s^{-1} and $N_0 = 4.5{\cdot}10^{19}$ m^{-2}. The relatively low value of the diffusion coefficient D indicates according to Hollenshead et al. [28] that the contaminants are relatively large, consisting of a large number of atoms. This consideration is also emphasized by the high value of σ_c, corresponding to large dissociation cross-sections in the range found by Alman et al. [26].

Fig. 4(b) illustrates the experimentally determined rate dt_c/dt of contamination growth and the change of the density of contaminants dn/dt at the border of the illuminated circle, which is calculated from the model with the parameters determined as before. Despite some oscillations in the derivative dt_c/dt caused by small variations of t_c, the contamination growth rate tends to a constant value, approaching stationarity. This corresponds to a stationary flux of contaminants into the irradiated zone, as indicated by the simulated curve dn/dt converging to zero. Notably, stationarity is reached for this setup only after tens of minutes, which is a much larger time scale than most of the recordings in electron microscopy.

4.3. Analysis of beam-showering for decreasing the density of contaminants

The model described in this work also applies to experiments with beam-showering performed to reduce the initial density of contaminants within a specified area. Fig. 5(a) shows the reference measurements without any previous beam-showering and the corresponding simulations of contamination growth after 5, 10, and 20 min irradiation in steps of 60 s with 28 s imaging time in between. A circle with a radius R = 620 nm was illuminated by a homogeneous electron beam with a current of j = 115 pA at 20 keV. The parameters of the reaction-diffusion process were determined as previously described by fitting the simulation to the experimental results and are indicated in the caption of the figure. Fig. 5(b) shows the same experiment, but after beam-showering for 1 min an area with the radius $R_{shower} = 7$ μm with a beam current of 3.4 nA, corresponding to a current density of 22 Am^{-2} to reduce the contaminant density in this region. The model indicates that even with this relatively high beam current, the contaminants were not removed completely, a fact attributed to additional adsorption from the residual gas atmosphere in the instrument. The modeled beam-showering process showed that at the beginning of the subsequent contamination growth measurements, 30 % of the initial density of contaminants still was present in the beam-showered area. The experiment for the contamination growth started then in the center of the showered area, like the preceding reference measurement. The parameters found for the reaction-diffusion process are indicated in the caption of the figure. Different from $\sigma_c = 2\cdot 10^{-20}$ m^2 from the reference contamination growth, here the interaction cross-section had to be set to a smaller value $\sigma_c = 7{\cdot}10^{-21}$ m^2 to fit the lower maximum and the less steep shape of the contamination curves at the border of the illuminated area. This reduction of σ_c might be explained by a change in the type of reactants within the two parts of the experiment. In the case of the reference measurements, the reactants mainly stem from the surface of the sample and connect to the higher value of σ_c. Their density is then locally reduced by beam-showering leading to a more pronounced supply of contaminants from the residual gas of the instrument tending to reestablish the initial equilibrium density of surface contaminants. The lower interaction cross-section adopted for this case could be a hint that the reactants from the residual gas are smaller than the initial surface

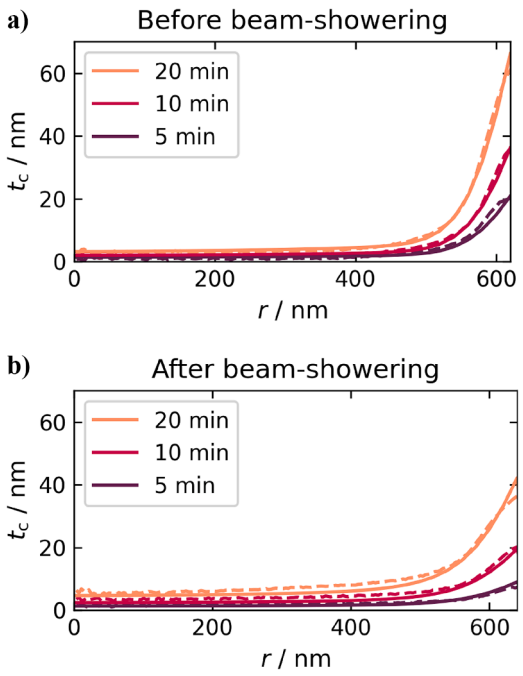

Fig. 5. Experimentally measured (dashed line) and simulated (solid line) contamination thickness t_c as a function of the distance r from the center, after irradiating an area with radius R = 620 nm for 5, 10, and 20 min. (a) Reference experiment without previous beam-showering. The simulated values were fitted to the experimental data by setting $D = 2\cdot 10^{-15}$ m^2s^{-1}, $\eta = 0.002$ s^{-1}, $\sigma_c = 2\cdot 10^{-20}$ m^2 and $N_0 = 6.5{\cdot}10^{19}$ m^{-2}. (b) Measured and simulated t_c after previous beam-showering an area with $R_{shower} = 7$ μm for 1 min with a current of 3.4 nA. The parameters of the subsequent contamination growth process were adjusted to $D = 2\cdot 10^{-15}$ m^2s^{-1}, $\eta = 0.002$ s^{-1}, $\sigma_c = 7\cdot 10^{-21}$ m^2, and a reduced initial density $0.3{\cdot}N_0$ ($N_0 = 6.5{\cdot}10^{19}$ m^{-2}) for the showered area to fit the experiments.

reactants, in conformity with the findings of Alman et al. [26]. This is also consistent with the dynamics of the inflow of contaminants analyzed below but needs additional investigations due to the contribution of further parameters.

The contamination thickness after beam-showering is lower than in the reference case as shown by the comparison of the corresponding t_c values in Fig. 5(a) and Fig. 5(b). The increased t_c after beam showering in the inner part of the illuminated area is explained by the analysis shown in context with Fig. 3(c) where this result is also found for reduced values of σ.

With the process parameters determined by reproducing the experimental results, the model can be used to better understand the time dependence of contamination growth and the flow of contaminants after previously beam-showering a larger area around the illuminating beam. Fig. 6(a) shows the relative density of contaminants n after distinct time intervals of irradiating an area with the radius marked in gray. The irradiation time of 60 s and the imaging time of 28 s give the time interval t_{img}= 88 s used in this figure for different curves describing n after 2, 5, 10, and 20 t_{img}. The rise of the curves in the region with $r < 7000$ nm by an offset similar to $\eta{\cdot}(1-n)$ shows that the depleted region fills up with contaminants from the residual gas. The change of the curve's gradient at around r = 7000 nm indicates the inflow from the unshowered area. Although the residual gas adsorption frequency is relatively low ($\eta = 0.002$ s^{-1}), this process dominates the contamination growth in the irradiated area ($r < 640$ nm) while the inflow from the outer unshowered regions does not reach this area during the considered time interval of 20 cycles. To better understand this process, no supply from the residual gas is assumed in the simulations by setting $\eta = 0$. Then the additive offset seen in Fig. 6(a) is suppressed and the diffusion of contaminants from outside of the showered area can be better

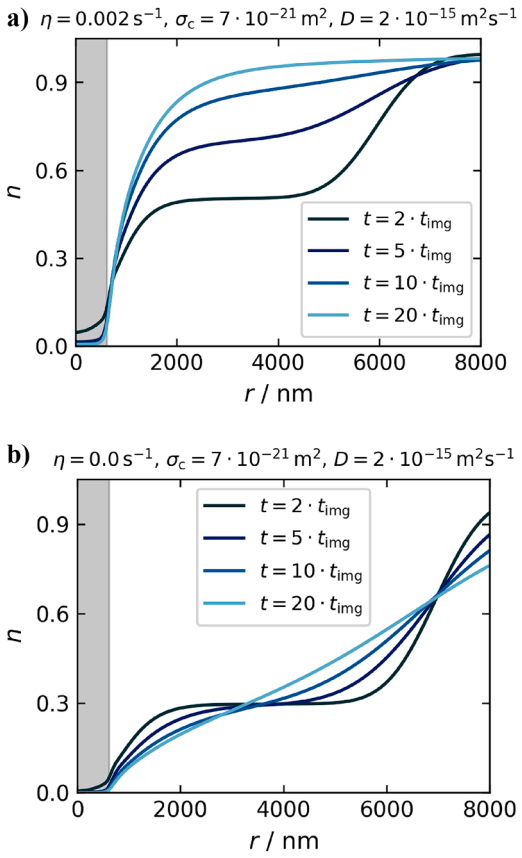

Fig. 6. Simulated temporal development of the relative contaminant density n as a function of the distance r from the center of the illuminated region with $r <$ 640 nm marked in grey. The contaminant density was reduced to 30 % of the initial N_0 in the showered area with the radius of $R = 7000$ nm. The time step $t_{img} = 88$ s is given by 60 s irradiating and 28 s imaging the region with contamination growth. (a) The residual gas acts as a source of contaminants. (b) Contribution from the residual gas is suppressed and surface diffusion is the only supply of contaminants.

distinguished by the dominant change of the gradient of the curves in Fig. 6(b). The inflow from the unshowered area reaches the irradiated central area only at the end of the analysis period at $t = 20\ t_{img}$ and less contamination grows due to the poorer supply of contaminants.

It is concluded that beam-showering reduces the contamination growth if performed in a large area around the irradiated region and with a high current to immobilize the surface contaminants. However, the reduction would be much more efficient, if the contribution of contaminants from the vacuum is substantially reduced, as shown by the considerations regarding Fig. 6(b).

5. Conclusions

To better understand the dynamical growth of contamination on surfaces illuminated by an electron beam, a time-dependent reaction-diffusion model was elaborated, considering the polymerization of contaminants on the sample surface provided by surface diffusion and from the instrumental residual gas atmosphere. The corresponding equation was solved numerically and reproduces the flow of contaminants and their interaction with the electron beam at distinct time intervals. This work aimed in particular to describe the beam-induced contamination growth by independent parameters and to reduce their number as much as possible. These parameters, which in general cannot be measured directly, were determined by comparing contamination experiments with the predictions of the model. The thickness and shape of the contamination patterns were determined at distinct time intervals by evaluating HAADF-STEM images taken at 20 keV and corresponding MC simulations. The unequivocal determination of the independent parameters resulted in $D = 2{\cdot}10^{-15}\ m^2s^{-1}$ for the diffusion coefficient of the surface contaminants and a supply frequency of contaminants $\eta = 0.002\ s^{-1}$ from the residual gas. The relatively low contribution from the vacuum shows that the main source of carbon contamination results from surface contaminants. Two values of $0.7{\cdot}10^{-20}$ and $2{\cdot}10^{-20}\ m^2$ were determined for the beam reaction cross-section σ_c. The lower value obtained from the beam-showering experiments indicates that smaller molecules from the residual gas atmosphere mainly contribute to the contamination growth instead of the previously depleted larger surface contaminants. The initial equilibrium surface density of contaminants was determined to be $N_0 = 4{\cdot}10^{19} - 6.5{\cdot}10^{19}\ m^{-2}$. Etching of contamination or desorption of contaminants by the beam can be included in the model but is interdependent with N_0 and was therefore ignored in this work.

The time dependency of the model allows the prediction of the flow of contaminants and the elaboration of measures for the reduction of contamination growth. It is shown that stationarity is reached for longer time intervals compared to typical imaging time scales in electron microscopy. For beam-showering, high current densities larger than 1 $nA/\mu m^2$ must be used to completely deplete initial surface contaminants in a large area around the subsequently irradiated region. This reduces the amount of contamination grown until the inflow of contaminants from outside of the depleted region reaches the irradiated area. A more pronounced reduction of contamination could be obtained by reducing the adsorption frequency of contaminants from the residual gas of the microscope, thus aiming for a better vacuum.

CRediT authorship contribution statement

Erich Müller: Writing – original draft, Software, Project administration, Methodology, Formal analysis, Conceptualization. **Katharina Adrion:** Validation, Investigation, Data curation. **Milena Hugenschmidt:** Writing – original draft, Validation, Formal analysis. **Dagmar Gerthsen:** Writing – original draft, Validation, Supervision, Formal analysis.

Declaration of competing interest

The authors declare that they have no known competing financial interests or personal relationships that could have appeared to influence the work reported in this paper.

Data availability

Data will be made available on request.

References

[1] H.G. Heide, Die Objektverschmutzung im Elektronenmikroskop und das Problem der Strahlenschädigung durch Kohlenstoffabbau, Z. Angew. Phys. 15 (1963) 116–128.
[2] R.F. Egerton, Radiation damage to organic and inorganic specimens in the TEM, Micron 119 (2019) 72–87.
[3] R.F. Egerton, C.J. Rossouw, Direct measurement of contamination and etching rates in an electron beam, Ournal Phys. Appl. Phys. 9 (1976) 659–663.
[4] R.L. Stewart, Insulating Films Formed Under Electron and Ion Bombardment, Phys. Rev. 45 (1934) 488–490.
[5] J.H.L. Watson, An Effect of Electron Bombardment upon Carbon Black, J. Appl. Phys. 18 (1947) 153–161.
[6] A.E. Ennos, The origin of specimen contamination in the electron microscope, Br. J. Appl. Phys. 4 (1953) 101–106.
[7] J. Hillier, On the Investigation of Specimen Contamination in the Electron Microscope, J. Appl. Phys. 19 (1948) 226–230.
[8] W.A. Knox, Contamination formed around a very narrow electron beam, Ultramicroscopy 1 (1976) 175–180.

[9] G. Love, N.M.T.Dennis Scott, L. Laurenson, Sources of contamination in electron optical equipment, Scanning 4 (1981) 32–39, https://doi.org/10.1002/sca.4950040105.
[10] L. Reimer, Scanning Electron Microscopy: Physics of Image Formation and Microanalysis, Springer, Berlin, Heidelberg, 1998.
[11] W. Li, D.C. Joy, Study of temperature influence on electron beam induced deposition, J. Vac. Sci. Technol. A 24 (2006) 431–436.
[12] J.J. Hren, Specimen contamination in analytical electron microscopy: Sources and solutions, Ultramicroscopy 3 (1978) 375–380.
[13] S. Hettler, M. Dries, P. Hermann, M. Obermair, D. Gerthsen, M. Malac, Carbon contamination in scanning transmission electron microscopy and its impact on phase-plate applications, Micron 96 (2017) 38–47.
[14] A. Kumao, H. Hashimoto, Shiraishi, Studies on Specimen Contamination by Transmission Electron Microscopy, J. Electron Microsc. 30 (1981) 161–170.
[15] D. Lau, A.E. Hughes, T.H. Muster, T.J. Davis, A.M. Glenn, Electron-beam-induced carbon contamination on silicon: characterization using Raman spectroscopy and atomic force microscopy, Microsc. Microanal. 16 (2010) 13–20.
[16] M. Amman, Atomic force microscopy study of electron beam written contamination structures, J. Vac. Sci. Technol. B Microelectron. Nanometer Struct. Process. Meas. Phenom. 14 (1996) 54.
[17] K. Rykaczewski, W.B. White, A.G. Fedorov, Analysis of electron beam induced deposition (EBID) of residual hydrocarbons in electron microscopy, J. Appl. Phys. 101 (2007) 54307.
[18] M. Hugenschmidt, K. Adrion, A. Marx, E. Müller, D. Gerthsen, Electron-Beam-Induced Carbon Contamination in STEM-in-SEM: Quantification and Mitigation, Microsc. Microanal. 29 (2022) 219–234.
[19] P. Schweizer, C. Dolle, D. Dasler, G. Abellán, F. Hauke, A. Hirsch, E. Spiecker, Mechanical cleaning of graphene using in situ electron microscopy, Nat. Commun. 11 (2020) 1743.
[20] K.H. Müller, Elektronen-Mikroschreiber mit geschwindigkeitsgesteuerter Strahlführung, Optik 33 (1971) 269–311.
[21] D.L. Freeman, J.D. Doll, The influence of diffusion on surface reaction kinetics, J. Chem. Phys. 78 (1983) 6002–6009.
[22] P. Hirsch, M. Kässens, M. Püttmann, L. Reimer, Contamination in a scanning electron microscope and the influence of specimen cooling, Scanning 16 (1994) 101–110.
[23] D.A. Smith, Elucidating the Growth Mechanisms of Electron Beam Induced Deposition via a Three Dimensional Monte-Carlo Based Simulation, 2007.
[24] I. Utke, P. Hoffmann, J. Melngailis, Gas-assisted focused electron beam and ion beam processing and fabrication, J. Vac. Sci. Technol. B Microelectron. Nanometer Struct. Process. Meas. Phenom. 26 (2008) 1197.
[25] W.F. van Dorp, C.W. Hagen, A critical literature review of focused electron beam induced deposition, J. Appl. Phys. 104 (2008) 81301.
[26] D.A. Alman, D.N. Ruzic, J.N. Brooks, A hydrocarbon reaction model for low temperature hydrogen plasmas and an application to the Joint European Torus, Phys. Plasmas 7 (2000) 1421–1432.
[27] C. Tian, C.R. Vidal, Cross sections of the electron impact dissociative ionization of CO, CH4 and C2H2, J. Phys. B At. Mol. Opt. Phys. 31 (1998) 895.
[28] J. Hollenshead, L. Klebanoff, Modelling radiation-induced carbon contamination of extreme ultraviolet optics, J. Vac. Sci. Technol. B Microelectron. Nanometer Struct. Process. Meas. Phenom. 24 (2006) 1023–1071, 64.
[29] K. Kanaya, E. Oho, N. Osaki, T. Oda, A contamination reducing method by ion beam bombardment of the specimen in high resolution electron microscopy, Micron Microsc. Acta 19 (1988) 163–173.
[30] S.J. Randolph, J.D. Fowlkes, P.D. Rack, Focused Nanoscale Electron-Beam-Induced Deposition and Etching, Crit. Rev. Solid State Mater. Sci. 31 (2006) 55–89.
[31] N. Agmon, Diffusion across proton collecting surfaces, Chem. Phys. 370 (2010) 232.
[32] J.D. Fowlkes, S.J. Randolph, P.D. Rack, Growth and simulation of high-aspect ratio nanopillars by primary and secondary electron-induced deposition, J. Vac. Sci. Technol. B Microelectron. Nanometer Struct. Process. Meas. Phenom. 23 (2005) 2825.
[33] C.J. Lobo, M. Toth, R. Wagner, B.L. Thiel, M. Lysaght, High resolution radially symmetric nanostructures from simultaneous electron beam induced etching and deposition, Nanotechnology 19 (2008) 25303.
[34] O. Dyck, S. Kim, S.V. Kalinin, S. Jesse, Mitigating e-beam-induced hydrocarbon deposition on graphene for atomic-scale scanning transmission electron microscopy studies, J. Vac. Sci. Technol. B 36 (2018) 11801.
[35] M.A. Giordano, G. Gutierrez, C. Rinaldi, Fundamental solutions to the bioheat equation and their application to magnetic fluid hyperthermia, Int. J. Hyperthermia 26 (2010) 475–484.
[36] Python (n.d.). https://www.python.org/.
[37] N. Silvis-Cividjian, C.W. Hagen, Electron Beam Induced Nanometer Scale Deposition, Adv. Imaging Electron Phys. 143 (2002) 1–235.
[38] Y. Lin, D.C. Joy, A new examination of secondary electron yield data, Surf. Interface Anal. 37 (2005) 895–900.
[39] L. Reimer, M. Wächter, Contribution to the contamination problem in transmission electron microscopy, Ultramicroscopy 3 (1978) 169–174, https://doi.org/10.1016/S0304-3991(78)80023-0.
[40] N. Ritchie, A New Monte Carlo Application for Complex Sample Geometries, Surf. Interface Anal. 37 (2005) 1006–1011.
[41] P. Chatwin, G. Dagan, J. List, C. Mei, S. Savage, P. Grathwohl, Diffusion in Natural Porous Media: Contaminant Transport, Sorption/Desorption and Dissolution Kinetics, Springer US, Boston, MA, 1998.